Fluid–solid boundary conditions for multiparticle collision dynamics

2010 J. Phys.: Condens. Matter 22 104106

(http://iopscience.iop.org/0953-8984/22/10/104106)

J. Phys.: Condens. Matter **22** (2010) 104106 (14pp) doi:10.1088/0953-8984/22/10/104106

Fluid–solid boundary conditions for multiparticle collision dynamics

Jonathan K Whitmer[1,2] **and Erik Luijten**[3,4]

[1] Department of Materials Science and Engineering, University of Illinois at Urbana-Champaign, Urbana, IL 61801, USA
[2] Department of Physics, University of Illinois at Urbana-Champaign, Urbana, IL 61801, USA
[3] Department of Materials Science and Engineering, Northwestern University, Evanston, IL 60208, USA
[4] Department of Engineering Sciences and Applied Mathematics, Northwestern University, Evanston, IL 60208, USA

Received 14 October 2009, in final form 30 December 2009
Published 23 February 2010
Online at stacks.iop.org/JPhysCM/22/104106

Abstract
The simulation of colloidal particles suspended in solvent requires an accurate representation of the interactions between the colloids and the solvent molecules. Using the multiparticle collision dynamics method, we examine several proposals for stick boundary conditions, studying their properties in both plane Poiseuille flow (where fluid interacts with the boundary of a stationary macroscopic solid) and particle-based colloid simulations (where the boundaries are thermally affected and in motion). In addition, our simulations compare various collision rules designed to remove spurious slip near solid surfaces, and the effects of these rules on the thermal motion of colloidal particles. Furthermore, we demonstrate that stochastic reflection of the fluid at solid boundaries fails to faithfully represent stick boundary conditions, and conclude that bounce-back conditions should be applied at both mobile and stationary surfaces. Finally, we generalize these ideas to create partial slip boundary conditions at both stationary and mobile surfaces.

(Some figures in this article are in colour only in the electronic version)

1. Introduction

Stochastic rotation dynamics (SRD) is a mesoscopic fluid simulation method developed a decade ago by Malevanets and Kapral [1, 2]. Since then, it has garnered considerable attention and is now, in its generalized form, commonly referred to as multiparticle collision dynamics (MPC). The coarse-graining of fluid elements into particle species that are governed by simplified interaction rules, in a manner that preserves fundamental conservation laws, leads to a significant acceleration of fluid simulations. When an MPC fluid is coupled to a molecular dynamics (MD) simulation of colloids, it permits the bridging of many timescales relevant to problems in colloidal physics [3] and can be used to represent the hydrodynamic interactions between colloids that result from their dispersion in a liquid medium. Recent examples include simulations of aggregate formation [4–7], particle sedimentation [3, 8, 9], bacteria swimming [10], membrane dynamics [11–14], and polymer translocation [15–17]. For a comprehensive review of the MPC method and for further applications, see [18] and [19].

Experimentally, colloids in suspension can exhibit of variety of interactions with the surrounding fluid. To enable the study of such systems, we examine various methods of imposing macroscopic fluid–solid boundary conditions in an MPC simulation. We first compare different options for treating stick boundary conditions at a fixed boundary, and then extend these to colloids, which have boundaries that move with respect to the solvent and are thermally coupled to it. In doing so we are able to address some issues that previous examinations of the boundary conditions have ignored. Further, we propose a simple but effective generalization of stick boundary conditions to obtain surfaces of arbitrary slip coefficient. This generalization is applicable to MPC simulations involving both stationary surfaces and surfaces of mobile spherical particles.

The MPC method consists of two steps: the *streaming* step, where particle positions and velocities are advanced in an MD manner, and the *collision* step, where fluid particle

momenta are mixed. The streaming step in MPC simulations is governed by the velocity-Verlet algorithm,

$$r_{i,j}(t+\delta t) = r_{i,j}(t) + v_{i,j}(t)\delta t + \tfrac{1}{2} f_{i,j}(t)(\delta t)^2, \quad (1)$$

$$v_{i,j}(t+\delta t) = v_{i,j}(t) + \tfrac{1}{2}[f_{i,j}(t) + f_{i,j}(t+\delta t)]\delta t, \quad (2)$$

where $r(t)$ and $v(t)$ are the position and velocity of a fluid particle at time t, and $f(t)$ is the total force exerted on the particle. The index i denotes the particle number, and the subscript j the dimensional component. Forces on fluid particles arise at fluid–solid boundaries, or due to an external field. However, interactions between fluid particles are wholly taken care of in the collision step. Here, a grid with lattice length a_0 is overlaid on the system, and fluid particles are partitioned into these cells. The velocities of the fluid particles are then updated by applying a randomly determined mixing operator $\mathbf{\Omega}$ to the relative velocity of each particle,

$$\mathbf{v}_i = \mathbf{v}_{\mathrm{cm},c_i} + \mathbf{\Omega}_{c_i}(\mathbf{v}_i - \mathbf{v}_{\mathrm{cm},c_i}). \quad (3)$$

Here, c_i is the cell containing particle i and $\mathbf{v}_{\mathrm{cm},c_i}$ denotes the center-of-mass velocity of the fluid particles in c_i. The mixing operator $\mathbf{\Omega}_{c_i}$ is chosen independently for each cell. In the original SRD algorithm, it is a rotation about a unit three-vector drawn from a uniform distribution.

The momenta can be mixed in many ways [20], so long as the correct macroscopic conservation laws are applied during the collision step. Mass is always conserved, as the number of fluid particles in each cell, and thus in the system as a whole, is fixed during the collision step. The remaining conservation laws are left to the choice of the operator $\mathbf{\Omega}$, although momentum must always be conserved by this operator. These two conditions are sufficient to ensure that in the large-scale limit this algorithm recovers the continuity and Navier–Stokes equations [15].

One must be careful applying the algorithm as constructed above, as it is not translationally invariant. This issue is due to the rigid grid imposed in the collision step, as was pointed out by Ihle and Kroll [21]. At low temperatures this is particularly evident, since particles will diffuse so slowly that they are effectively trapped in the same cell, colliding with the same set of particles for many time steps. This violates molecular-chaos assumptions and leads to velocity-dependent transport coefficients in the fluid. At high temperatures, this problem does not arise, since the particles diffuse rapidly enough between different cells and thus collide with different sets of neighbors. A general solution to this problem is to restore Galilean invariance by shifting the origin of the grid by a random vector with components in $[0, a_0)$ prior to sorting the fluid particles into cells in each collision step [21].

In our discussion of the MPC model we follow the notation of [22], which we will briefly reiterate here for completeness. A simulation of the MPC model involves the following set of parameters: the number of fluid particles per cell γ, the time between collision steps Δt_c (usually chosen as an integer multiple of the molecular dynamics evolution time step δt), the collision cell size a_0, the linear system size L, the particle mass m_f, and the temperature T. A natural system of units arises if a_0 is chosen as the unit length and m_f as the unit mass, and Boltzmann's constant k_B is set to unity. The characteristic velocity is then the thermal velocity of the fluid particles, $v_0 = \sqrt{k_B T/m_f}$, and $t_0 = a_0/v_0$ represents a characteristic time. This in turn defines the dimensionless mean free path $\lambda = \Delta t_c/t_0$, the characteristic viscosity $\eta_0 = \sqrt{k_B T m_f}/a_0^2$, and the unit of acceleration $g_0 = a_0/t_0^2$. When colloidal particles or additional fluid species are added to this system, a new set of mass and length scales is introduced (notably the colloid mass M_c, colloid–colloid diameter σ_{cc}, and colloidal radius a). These can be incorporated naturally by defining masses in terms of m_f and length scales in terms of a_0 [22]. Finally, the collision operator $\mathbf{\Omega}$ must be specified. The consequences of this choice have been examined in detail in [20, 23]. In our simulations, we employ both the original SRD collision rule [1], as well as the Andersen thermostat (AT) collision rule [20]. In addition to the mandatory conservation of mass and momentum, the SRD method conserves energy, whereas the AT method applies a local thermostat to the fluid in each collision cell. The use of a thermostat implies that energy conservation is no longer fulfilled, although it is retained in a statistical sense. Both of these rules have recently been extended to angular-momentum conserving algorithms [20].

In studying various boundary conditions on MPC fluids, we seek the optimal rules for studying embedded colloidal particles. To do this, we examine methods for modeling stick boundary conditions at stationary walls that have been presented previously, and extend them to include partial slip effects. Finally, we examine consequences of these methods for simulating suspended colloidal particles.

2. Viscosity in an MPC fluid

The viscosity coefficients of a fluid are a measure of its resistance to deformations. This can be quantified by means of the viscous stress tensor σ_{ij}. For Newtonian fluids, the stress tensor is a linear combination of the spatial derivatives of the fluid velocity $\mathbf{u}$ [24], the most general of which is [20, 25]

$$\sigma_{ij} = \hat{\eta}(\partial_{x_i} u_j + \partial_{x_j} u_i) + \bar{\eta}(\partial_{x_i} u_j - \partial_{x_j} u_i) + \eta_b(\partial_{x_k} u_k)\delta_{ij}. \quad (4)$$

Here $\hat{\eta}$, $\bar{\eta}$, and η_b are the symmetric, antisymmetric, and bulk viscous contributions, respectively. In most situations we consider the flow of incompressible fluids which conserve angular momentum, where only the symmetric contribution $\hat{\eta}$ is nonzero. For unidirectional shear, this leads to a standard relation between the stress tensor and the viscosity (now indicated generically as η),

$$\sigma_{ij} = \eta\dot{\gamma}. \quad (5)$$

Here, $\dot{\gamma} = \partial_{x_i} u_j$ is the shear rate. The stress tensor in equation (5) can in turn be related to the flux of x_j-momentum across planes of constant x_i.

Even in the absence of angular-momentum conservation viscosity can still be defined as in equation (5), provided the stress tensor only enters the equations of motion through its divergence in the Navier–Stokes equations. For incompressible fluids, the divergence of the stress tensor simplifies to

$$\partial_{x_i}\sigma_{ij} = (\hat{\eta} + \bar{\eta})\partial_{x_i}^2 u_j, \quad (6)$$

and $\eta = \hat{\eta} + \bar{\eta}$ is the effective viscosity. In addition, the antisymmetric term is important for boundary conditions if the fluid velocity is related to the tangential stress [25, 26], although velocity-based boundary conditions (such as those that we will consider for Poiseuille flow) remain unaffected. It should also be noted that the MPC fluid has an ideal-gas equation of state [18] and thus is not incompressible. If compressibility effects are strong, explicit inclusion of all three terms in equation (4) is necessary. In the MPC fluid these effects can be minimized by ensuring that the Mach number relating flow velocity to the speed of sound, $\mathrm{Ma} = v_\mathrm{f}/c_\mathrm{s}$, is small [22]. Alternatively, attempts have been made to reduce compressibility effects by incorporating a non-ideal equation of state [27, 28].

One can calculate the viscosity of an MPC fluid by observing how momentum is transported through the fluid. Momentum can be transferred in two ways, corresponding to the two steps of the MPC algorithm. During the streaming step, momentum is carried by each particle in its direction of motion. During the collision step, momentum is redistributed among particles in a collision cell. This results in two contributions to the viscosity of an MPC fluid that depend strongly on the particle density and on the time between collisions. At small mean free path lengths, momentum transfer via collisions is the dominant contribution to the viscosity, whereas at large λ the streaming of particles dominates. If the mean free path length is large enough to justify the molecular-chaos assumption, the viscosity of the SRD model can be calculated analytically [29–32], permitting an accurate test of simulation data. More recently, analytical results for the viscosity have been obtained for other choices of the multiparticle collision operation as well [20].

3. Stick and slip boundary conditions

Fluid flow is strongly affected by the presence of interfaces. For fluids in contact with a solid phase, the normal component of the velocity at the interface must be zero, whereas the tangential velocity inherently depends on molecular interactions at the interface. Two ideal scenarios are those of stick and slip boundary conditions. For stick (or 'no-slip') boundary conditions, the tangential velocity of the fluid relative to that of the boundary vanishes at the interface. For slip boundary conditions, the tangential velocity of the fluid is unaffected by the presence of the interface. Most real surfaces satisfy a partial slip condition, which lies between the two [26, 33, 34]. In this case, the relative tangential velocity of the fluid is diminished near the surface, but remains nonzero. The amount of slip can be quantified via the *slip length*, which is the (hypothetical) distance into the surface at which the relative tangential velocity would be zero. For shear flow in the x-direction relative to a boundary at $z = 0$, this yields

$$\lambda_\mathrm{slip} = \frac{u_x(0)}{\partial_z u_x(0)}. \tag{7}$$

Note that for perfect slip boundaries λ_slip diverges. The importance of slip in a macroscopic system can be expressed through the effective Knudsen number [34]. The conventional Knudsen number is defined as the ratio between mean free path length and a representative physical length scale of the system, and is useful for quantifying the viscous character of a flow. Here we define it as the ratio between slip length and system size,

$$\mathrm{Kn} = \frac{\lambda_\mathrm{slip}}{L}. \tag{8}$$

From this definition, in combination with the notion of slip length as a distance in the surface at which stick boundary conditions would apply, we see that a small Knudsen number implies that stick boundary conditions are a good approximation for the system. In physical systems, slip notably arises from hydrophobicity or surface roughness [26, 33, 34], and often is not evident unless the system size is on the order of microns. In addition, the viscosity near a surface may be altered if a fluid contains a surface-active component, or if fluid–solid interactions near the interface modify the local composition of the fluid. A lowered viscosity facilitates the motion of monolayers near the interface, resulting in a so-called apparent slip boundary condition.

Likewise, slip in an MPC fluid can be either intentional or apparent. As will be discussed below, modifying the exchange of tangential momentum between fluid and solid makes it possible to change the macroscopically determined slip length in a controlled way. This can in turn be mapped onto an effective Knudsen number. However, one must be mindful that simulation artifacts can affect the boundary conditions as well. Specifically, the presence of *partially filled* collision cells [18, 35], either due the shape of boundaries or due to the Galilean-invariant lattice shifting, leads to a decreased viscosity at the surface resulting in an apparent slip.

4. Incorporating boundary conditions in an MPC fluid

Within a particle-based simulation, there are several ways to incorporate physical objects, such as walls. The simplest method is to represent a wall by means of a repulsive potential that only varies perpendicular to the plane defining the wall, and include the resulting forces in the Verlet update step. Since such a potential cannot affect the tangential velocity of the fluid, this implementation results in perfect slip boundary conditions. To represent stick boundary conditions, a mechanism is needed to decrease the relative tangential velocity of the fluid at the wall. One possibility is to implement a noncentral force on particles near the wall. In principle, this will make it possible to create boundary conditions with arbitrary slip by removing some fraction of the particle momenta near a solid surface in each time step. In this paper, we do not examine force-based conditions, but instead impose *hard* walls that reflect incoming fluid particles. Regular, specular reflections constitute the counterpart of a repulsive potential and lead to perfect slip boundary conditions. Other boundary conditions can be created through bounce-back conditions, where momentum is exchanged as an impulse between the fluid and the solid. In this section, we review several choices for the reflection rules, and consider their generalization from stationary walls to moving fluid–solid interfaces.

4.1. Bounce-back conditions

The bounce-back boundary condition was first proposed for MPC simulations by Malevanets and Kapral [1]. It is a direct analog of the stick boundary condition often applied in lattice-Boltzmann simulations [36], and functions by controlling the momentum flux at the boundary. This condition is implemented as follows. If, at the end of a streaming step (Verlet update), a fluid particle with velocity $\mathbf{v}$ is found to overlap with a wall that has a velocity $\mathbf{v}_{\text{surface}}$, we determine the intersection of its trajectory and the surface and restore the particle to the time and position of contact. Then, the velocity of the particle relative to the surface, $\tilde{\mathbf{v}} \equiv \mathbf{v} - \mathbf{v}_{\text{surface}}$, is *completely* reversed ($\tilde{\mathbf{v}} \to -\tilde{\mathbf{v}}$) and for the remainder of the Verlet step the particle is propagated from the point of contact using its new velocity. As a result, the average relative velocity of the fluid near the wall is zero, since the relative velocity distribution of particles reflected from the wall mirrors the corresponding distribution of particles approaching the wall.

For the case of a solid boundary in motion (e.g., a colloid) one must determine a suitable location at which to apply the boundary condition, as the point of contact between a colloid and a fluid particle depends on the trajectory of both. For simulations of a colloid embedded in a solvent, we use the following prescription [37]: if fluid particles are found to overlap with a colloid at the end of the streaming step, we restore all participating fluid particles, as well as the colloid, to their positions one half Verlet time step earlier. This configuration is then treated as the point of contact and velocity reflections are performed accordingly. The changes in momentum and angular momentum of the affected fluid particles relative to the center of the colloid are summed and used to update the instantaneous linear and angular momentum of the colloid. Subsequently, the fluid particles and the colloid are propagated for the second half of the time step. If this results in the overlap of additional fluid particles with the colloid, the procedure is repeated, i.e., the particles are restored to their positions halfway the second half-step and another reflection operation is performed. This process is iterated until either no new overlaps occur or a threshold number of iterations is reached. In practice, only a few iterations are necessary. In this method, it is assumed that fluid particles do not simultaneously overlap with more than one colloid. This can be guaranteed by choosing σ_{cc} slightly larger than $2a$, similar to the method utilized in [8, 22] to compensate for spurious depletion attractions between colloids.

When implementing bounce-back conditions, one must be careful to ensure that complicated geometries are treated properly. For example, the time step δt must be sufficiently small to ensure that fluid particles cannot pass through small features in a wall or through a colloid. Also, interactions with multiple walls over the course of a single time step (e.g., reflections in the corner of a box) require additional consideration. If the point of contact can be determined exactly this simply involves iterative application of the bounce-back rule for static interfaces. Otherwise, rules similar to the colloidal rule discussed above may be applied.

4.2. Stochastic conditions

Stochastic boundary conditions were proposed for two-dimensional simulations of suspended solids by Inoue *et al* [38], and later applied to the three-dimensional motion of spherical colloids by Padding *et al* [37]. These conditions are intended as an alternative to the bounce-back conditions of section 4.1, providing a simple implementation of stick boundary conditions for moving objects.

In this method, the point of contact in a fluid–colloid collision is determined in the same manner as for the dynamic rule discussed in the previous section, but the new relative fluid velocities are obtained from a half-space Maxwell–Boltzmann distribution rather than from direct velocity reversals. The tangential components of the relative velocity are drawn from a Gaussian distribution with zero mean and standard deviation v_0. The normal component is drawn from a degree-2 Weibull distribution with mean v_0 and standard deviation v_0. Thus, energy conservation is replaced with the use of a thermostat, an approximation that can be justified if $\lambda a_0 \ll \sigma_{\text{cc}}$ [5, 38]. A variation of the stochastic condition [17] permits fluid particles to freely enter solid regions, where the particle velocities are then modified to follow a Maxwell–Boltzmann distribution about the solid-body velocity. This boundary condition, however, allows flow to penetrate small objects [25] and hence is not considered here.

In simulations of colloidal diffusion employing stochastic boundary conditions it was found that the autocorrelation functions of the linear and angular velocity were well represented by theoretical predictions for colloids with stick boundary conditions [37]. However, since it is difficult to accurately test for the presence of slip in a spherical geometry, we examine the validity of this rule for plane Poiseuille flow in section 6.1. To our knowledge, such tests were not done previously.

4.3. Mixed bounce-back conditions

We observe that, in analogy with the idea of noncentral forces, it is possible to control the degree of slip at a wall using bounce-back conditions. Thus, we propose to generalize these conditions by tuning the average amount of tangential momentum transferred to a surface in a collision. We examine two possible implementations. In *Method 1*, each particle that impinges on a solid surface undergoes a fixed fractional change in its relative tangential velocity determined by a parameter Γ. For a fluid particle with relative velocity $\tilde{\mathbf{v}}$ (defined in section 4.1), its post-collision velocity $\mathbf{v}'$ is related to the pre-collision velocity $\mathbf{v}$ by

$$\tilde{\mathbf{v}}'_n = -\tilde{\mathbf{v}}_n, \tag{9}$$

$$\tilde{\mathbf{v}}'_t = (2\Gamma - 1)\tilde{\mathbf{v}}_t. \tag{10}$$

The subscripts n and t refer to the normal and tangential components of the velocity at the point of contact. This method interpolates between bounce-back conditions ($\Gamma = 0$) and specular reflection ($\Gamma = 1$). It should be noted that these boundary conditions do not conserve energy for $\Gamma \notin \{0, 1\}$. If the solid is assumed large enough to

maintain an internal temperature despite absorbing energy from the fluid, dissipation is not an issue if an appropriate thermostat is applied to the fluid. However, energy dissipation could present complications for colloidal particles. As an alternative, in *Method 2* all fluid–solid collisions are performed using either perfect stick boundary conditions (the bounce-back condition of section 4.1) or perfect slip boundary conditions (i.e., specular reflection), so that boundary interactions always conserve energy. For each collision, the applied boundary condition is determined at random: bounce-back collisions have a probability $1 - \Gamma$ and specular reflections occur with a probability Γ. In spirit, this is very similar to an analytical approach to generalize the 'rough-sphere model' for the orientational relaxation of spherical particles with stick boundary conditions to spheres with arbitrary roughness [39]; comparable ideas have recently been proposed for implementing partial slip in lattice-Boltzmann simulations [40]. In case of interaction with a colloid, bounce-back collisions lead to the transfer of tangential as well as normal momentum, whereas specular reflections involve only the transfer of normal momentum. We examine both Method 1 and Method 2 in section 6.2.

5. Collision rules to remove spurious slip

The bounce-back condition was studied in detail by Lamura and Gompper in two dimensions [35, 41], and has been applied in three-dimensional systems as well [25, 42]. In studying the steady Poiseuille flow profile, it was found that the bounce-back rule of section 4.1 is not sufficient to guarantee absence of slip at the walls. This problem arises from the intersection of MPC cells with the solid surface, which results in boundary cells that contain fewer fluid particles than their bulk counterparts. Whereas the streaming contribution to the viscosity is not affected by this, the collisional viscosity in boundary cells is diminished, lowering the total viscosity compared to its bulk value. We illustrate this for cells intersected by a planar wall in appendix A. Here, we review several modifications to the collision step of the MPC method that have been proposed to rectify this issue.

5.1. Bulk filling rule

The earliest solution, denoted here as the bulk filling rule (BFR), is due to Lamura and Gompper [35] and has found rather wide-spread application. In this rule, pseudoparticles with Maxwell–Boltzmann distributed velocities are added to underfilled boundary cells (i.e., boundary cells with $N_{\text{fluid}} < \gamma$ fluid particles) in order to match the bulk particle density. The inclusion of these pseudoparticles (which can be represented by a single particle of mass $(\gamma - N_{\text{fluid}})m_{\text{f}}$) in the collision step increases the effective viscosity.

It should be noted that the number of fluid particles in each cell fluctuates. Since, according to this rule, only underfilled boundary cells are modified, the resulting average particle density in boundary cells is *higher* than in bulk cells. To remove this asymmetry, we propose a variation of this rule, in which for wall cells with $N_{\text{fluid}} > \gamma$ fluid particles the center-of-mass velocity is modified by *subtracting* the velocity of a pseudoparticle,

$$\mathbf{v}'_{\text{cm}} = \frac{1}{\gamma}[N_{\text{fluid}}\mathbf{v}_{\text{cm}} - (N_{\text{fluid}} - \gamma)\mathbf{v}_{\text{MB}}], \tag{11}$$

where $\mathbf{v}_{\text{MB}}$ is drawn from a Maxwell–Boltzmann distribution for a particle with mass $(N_{\text{fluid}} - \gamma)m_{\text{f}}$. We refer to this as the symmetrized bulk filling rule (SBR).

5.2. Alternative collision rules

Reference [35] also considered the possibility of adding *stationary* pseudoparticles to underfilled boundary cells. This approach was observed to result in an increased particle density near the walls, which can be understood by noting that it corresponds to a zero-temperature representation of the walls. Accordingly, the walls act as heat sinks that decrease the particle velocities and localize the particles near the walls. Although this unintended consequence may render this approach unusable, it is conceivable that the application of a thermostat alleviates the problem. For this reason, we will review its performance in section 6.1. However, in analogy with the SBR proposed in section 5.1 we introduce the following symmetric variant. If the number of particles in a boundary cell N_{fluid} differs from the bulk number of particles per cell γ, the center-of-mass velocity is rescaled by a factor N_{fluid}/γ. If $N_{\text{fluid}} < \gamma$ this is equivalent to the addition of stationary pseudoparticles. We refer to this as the simple rescaling rule (SRR).

In [25], it was proposed to place randomly distributed pseudoparticles within the parts of boundary cells that overlap with the solid. The velocity of each pseudoparticle is drawn from a Maxwell–Boltzmann distribution centered around the velocity of the wall at the particle position. As in the other rules involving pseudoparticles, their density is equal to the bulk particle density. However, rather than on a cell-wise basis, we choose the *total* number of pseudoparticles according to the total overlap volume of boundary cells with solid regions in the system. This has the benefit that the fluctuations in the number of pseudoparticles per cell approximate the cell-wise fluctuations in the bulk particle density. This collision rule, which we refer to as the virtual particle condition (VPC), allows a natural extension to angular-momentum conserving implementations of the MPC algorithm, since pseudoparticles have both position and velocity, unlike pseudoparticles in the BFR [25]. A potential complication in the VPC is that it can be computationally costly to disperse pseudoparticles in solids with complex geometry.

When determining velocities in the virtual particle condition in combination with the mixed bounce-back rule proposed in section 4.3 for surfaces with partial slip, we employ the slip parameter Γ. The velocity of a pseudoparticle at position $\mathbf{r}$ within the rigid body is drawn from a Maxwell–Boltzmann distribution centered around an average velocity

$$\langle \mathbf{v} \rangle = \Gamma \langle \mathbf{v}_{\text{avg}} \rangle + (1 - \Gamma)\mathbf{v}(\mathbf{r}), \tag{12}$$

where $\mathbf{v}(\mathbf{r})$ denotes the rigid-body velocity at the position $\mathbf{r}$ and $\langle \mathbf{v}_{\text{avg}} \rangle$ is the average of the real fluid particle velocities in the boundary cell. For perfect stick boundary conditions ($\Gamma = 0$) this reduces to a distribution centered around the local rigid-body velocity, whereas for perfect slip boundary conditions ($\Gamma = 1$) the average velocity of the pseudoparticles matches the local fluid flow.

5.3. Notes on collision rules for moving boundaries

The generalization of the rules in this section to moving solids poses some problems. For example, in the BFR (section 5.1) pseudoparticle velocities may be drawn from a Maxwell–Boltzmann distribution whose average velocity is the solid-body surface velocity in that cell. For an object with center-of-mass position $\mathbf{r}_{\text{cm}}$, center-of-mass velocity $\mathbf{v}_{\text{cm}}$, and angular velocity $\boldsymbol{\omega}$, the surface velocity at position $\mathbf{r}$ is given by

$$\mathbf{v}_{\text{surface}}(\mathbf{r}) = \mathbf{v}_{\text{cm}} + \boldsymbol{\omega} \times (\mathbf{r} - \mathbf{r}_{\text{cm}}). \tag{13}$$

The average surface velocity can be obtained by Monte Carlo integration of $\mathbf{v}_{\text{surface}}$ over the manifold of intersection between the solid surface and the MPC cell. In the limit of a stationary wall, this reduces to the stationary BFR, so we would expect similar slip behavior from this rule. When this approach is applied to colloids, momentum gained by the pseudoparticles during the collision step must be explicitly accounted for to ensure our system conserves momentum. Since pseudoparticles are located inside the colloidal surface, it is natural to add this momentum to the colloid. If F denotes the set containing all pseudoparticles i interacting with colloid j, the net momentum changes are

$$\Delta \mathbf{P}_j = -\sum_{i \in F} m_{\text{f}} \Delta \mathbf{v}_i, \tag{14}$$

$$\Delta \mathbf{L}_j = \sum_{i \in F} m_{\text{f}} \Delta \mathbf{v}_i \times (\mathbf{r}_i - \mathbf{r}_j). \tag{15}$$

Here $\mathbf{P}_j$ and $\mathbf{L}_j$ are the colloid's linear and angular momentum, respectively, and $\Delta \mathbf{v}_i$ is the change in velocity of fluid particle i during the collision step. Conceptually, this momentum transfer is only correct in case of perfect stick boundary conditions, a notion that we will address in section 7. Alternatively, one can restore momentum conservation by compensating the change in momentum and angular momentum (if using an angular-momentum conserving rule) of the pseudoparticles in each collision step by an equal and opposite change in the real fluid particles in that cell. However, this process amounts to neglecting the pseudoparticles entirely and thus offers no improvement over standard bounce-back conditions for removing spurious slip.

6. Plane Poiseuille flow

In this section, we investigate the performance of the bounce-back and stochastic boundary conditions reviewed in section 4 in combination with the various methods for removing spurious slip reviewed in section 5. We do so in a simulation of fluid flow between two parallel stationary walls, where the fluid experiences a constant pressure gradient or a uniform body force (e.g., gravitation). This plane Poiseuille flow has the advantage that the velocity profile is known analytically, even when slip is present [24, 43].

Assuming a low Mach number, we can apply the (incompressible) Navier–Stokes equations,

$$\rho(\partial_t + \mathbf{u} \cdot \nabla)\mathbf{u} = -\nabla p + \eta \nabla^2 \mathbf{u} + \rho \mathbf{g}, \tag{16}$$

$$\nabla \cdot \mathbf{u} = 0, \tag{17}$$

where ρ is the fluid density, p the (spatially dependent) fluid pressure and $\mathbf{g}$ the acceleration resulting from an external force on the fluid. Upon alignment of the Cartesian coordinates such that $\hat{x}$ is the direction of flow and $\hat{y}$ is perpendicular to the two walls, this reduces to a two-dimensional problem. When stick boundary conditions are imposed at $y = 0$ and $y = L$, the steady-state solution ($\partial_t \mathbf{u} = 0$) yields the well-known parabolic profile

$$u_x(y) = \frac{-\Delta p + \rho g}{2\eta}(L - y)y. \tag{18}$$

Here, Δp is the magnitude of the pressure gradient and $g = |\mathbf{g}|$. In the case of uniform slip at both walls, we can utilize the boundary condition equation (7) (with y replacing z and a corresponding condition at $y = L$) and obtain the same velocity profile with the addition of a constant velocity across the channel [34],

$$u'_x(y) = \frac{-\Delta p + \rho g}{2\eta}(L - y)y + \frac{(-\Delta p + \rho g)\lambda_{\text{slip}} L}{2\eta}. \tag{19}$$

6.1. Results for plane Poiseuille flow

Our simulations employ an MPC fluid with the SRD collision rule. We use $\gamma = 32$ particles per cell in a rectangular geometry $25a_0 \times 25a_0 \times 50a_0$, similar to the systems examined in [42]. The rotation angle in the SRD operator is set to $\alpha = \pi/2$ and the mean free path length equals $\lambda = 0.2$, resulting in a viscosity $\eta = 10.91\eta_0$. Flow strength is controlled by a gravitational force on the fluid particles, with $g = 0.005 g_0$. Because the gravitational force imparts energy to the system, a thermostat is required. We use both Galilean-invariant global velocity rescaling [22] and a simple extension of this thermostat in which the rescaling parameter is calculated on a cell-wise basis.

As illustrated in figure 1, all simulations lead to a parabolic velocity profile, but there are important differences between the results obtained from different algorithms. As noted earlier for a two-dimensional implementation [35], the bounce-back condition of section 4.1 (filled squares), when applied without special treatment of the boundary cells, leads to significant slip at $x = 0$ and $25a_0$ and a velocity profile that is enhanced compared to the theoretical prediction (equation (18)) across the entire channel width. Application of the BFR (open squares) removes the slip, but an enhancement of the velocity profile away from the walls remains, contrary to what was found for two-dimensional flow [35]. We believe that this can be explained from the use of our velocity rescaling scheme.

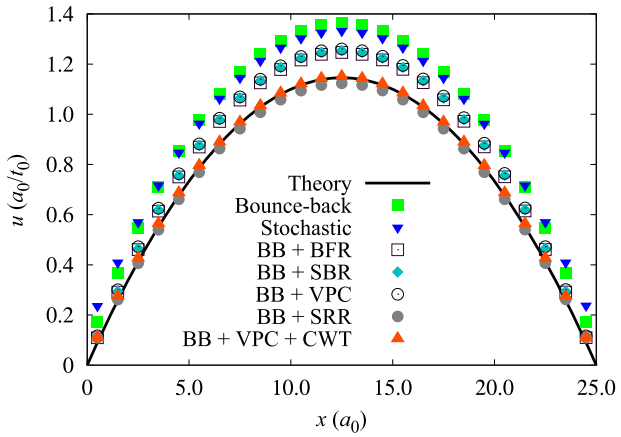

Figure 1. Comparison of plane Poiseuille flow profiles for various boundary conditions defined in section 5. All simulation data were obtained use the bounce-back condition (BB), except those indicated as 'stochastic'. See the text for a detailed discussion of each method. Except for 'BB + VPC + CWT', the key lists all data sets in order of decreasing magnitude of the velocity profile. The data sets for 'BB + BFR' (open squares), 'BB + SBR' (diamonds), and 'BB + VPC' (open circles) lie almost exactly on top of each other for all x.

Since the real fluid particles in boundary cells experience a net flow, pseudoparticles that participate in the fluid collision step will remove momentum and energy from these cells, leading to a local temperature decrease during the collision step. Fluid in the bulk cells remains at the correct temperature, as the SRD collision rule conserves energy. Thus, subsequent global velocity rescaling performed by the thermostat leads to an overheating of the bulk fluid and a consequent decrease in the viscosity. This effect can be suppressed by choosing smaller cells, so that the fluid particles in the boundary cells have a smaller net velocity. The symmetric version of this rule, SBR (filled diamonds), yields almost identical results. This can be understood from the fact that *overfilled* boundary cells occur very rarely. For the stationary walls examined here, the virtual particle condition of section 5.2 (open circles) only differs from SBR in the manner in which the pseudoparticles are distributed over the boundary cells (i.e., fluctuations in the total number of particles and pseudoparticles per cell are permitted in VPC, but do not occur in SBR). The resulting velocity profile is indeed indistinguishable from that obtained via SBR. Apart from the deviations ascribed to the global thermostat, it is noteworthy that BFR, SBR, and VPC all properly remove the spurious slip at the walls.

The last rule applied in conjunction with the bounce-back condition, SRR (filled circles), appears to match the analytical prediction remarkably well. However, this is a spurious effect, in which the velocity enhancement resulting from the thermostat coincidentally cancels the suppression of the velocity profile one would otherwise observe when using this rule. For other parameter choices, the agreement disappears. Conversely, we found excellent agreement with the theoretical velocity profile for BFR, SBR, and VPC when decreasing the magnitude of the gravitational driving force or increasing the mean free path length λ (keeping in mind limitations on the Mach number).

On the other hand, the spurious velocity enhancement completely disappears, *independently* of parameter choice, upon application of a cell-wise thermostat (data indicated as VPC + CWT in the graph, filled triangles). Here, the velocity rescaling factor is calculated per cell, based upon the strength of the velocity fluctuations about the mean particle velocity in each cell. The distinction between a global and a cell-wise thermostat only applies to the SRD collision rule. In an MPC fluid with the AT collision rule, all cells are thermostatted individually in the collision step. Therefore, we have chosen to exclusively employ the MPC-AT fluid in sections 6.2 and 7. Note, however, that spurious slip is still present in these simulations unless corrected for by, e.g., the VPC.

Lastly, we have also tested the stochastic bounce-back condition of section 4.2 (inverted filled triangles). This condition was specifically proposed to be used without pseudoparticles to facilitate the treatment of complex, moving geometries. However, as illustrated in figure 1, the resulting velocity profile suffers from even greater spurious slip than the profile obtained with the standard bounce-back condition. Indeed, this slip persists even if pseudoparticles are added to the collision step (not shown). This appears to be in contradiction with the agreement found in colloid simulations employing this method and analytical predictions of velocity autocorrelation functions [37]; we will elucidate this discrepancy in section 7.3 and appendix B.

6.2. *Plane Poiseuille flow with partial slip*

Having established the performance of the bounce-back condition in conjunction with various collision rules, we now proceed to investigate the mixed bounce-back rules proposed in section 4.3 for the implementation of partial slip boundary conditions.

We use an MPC-AT fluid with a system geometry and particle density identical to those in section 6.1. The mean free path length is set to $\lambda = \sqrt{2}$ (yielding a viscosity $\eta = 25.91\eta_0$) and the driving force corresponds to $g = 0.01g_0$. The slip coefficient Γ is varied from 0 (stick boundary conditions) to 0.9 (near perfect slip). For both methods described in section 4.3 we confirm that the degree of slip can be increased monotonically by increasing Γ. In accordance with equation (19), we obtain the same parabolic velocity profile for all choices of Γ, shifted by an additive constant that depends only on the effective Knudsen number (equation (8)) and the maximum channel velocity $u_{\max} \equiv u_x(L/2)$ (cf equation (18)). Figure 2 illustrates this for simulation results obtained by means of Method 2 (in which the bounce-back condition and specular reflection are mixed with probabilities $1 - \Gamma$ and Γ, respectively) without the application of any pseudoparticles.

The effective Knudsen number corresponding to these results is plotted in figure 3. To clarify the apparent slip resulting from the omission of pseudoparticles, we also determine Kn in simulations with fixed $\Gamma = 0$ as a function of cell resolution in systems of dimension $L \times L \times 2L$. We maintain the values for particle density and mean free path length, while increasing the number of cells across the channel width by increasing L. Simultaneously, we decrease

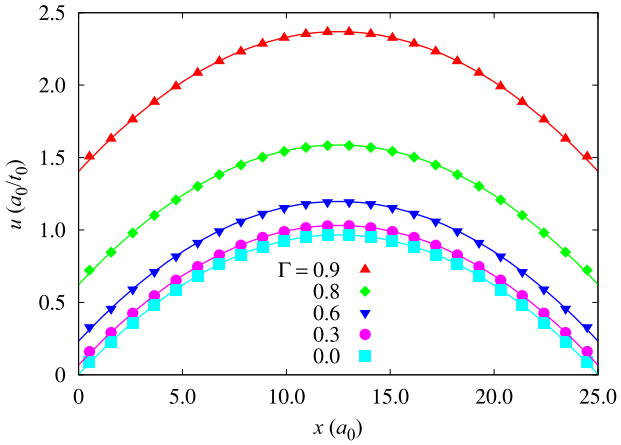

Figure 2. Slipping Poiseuille flow profiles in a channel of width $25a_0$. The slip coefficient is varied from $\Gamma = 0$ (stick boundary conditions) to 0.9 (near perfect slip). For clarity, some of the profiles are omitted.

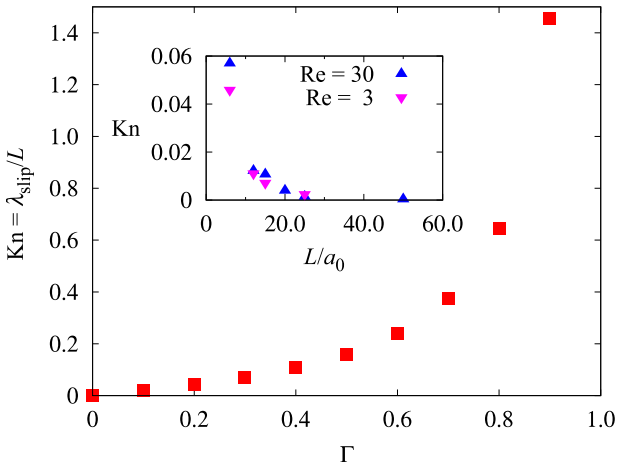

Figure 3. Effective Knudsen number Kn as a function of slip parameter Γ. Note how Kn diverges as Γ approaches unity. *Inset*: Knudsen number as a function of channel resolution L/a_0. In these simulations, $\Gamma = 0$ and the gravitational constant is varied as $1/L^3$ to maintain a constant Reynolds number Re (see text). For both Re = 3 and 30, Kn tends toward 0 as the resolution is increased, confirming that apparent slip can be mitigated by increasing the cell resolution in MPC simulations.

the gravitational constant such that the Reynolds number, $\mathrm{Re} = \rho u_{\max} L/\eta$, remains constant. This is equivalent to variation of the cell resolution, since systems with equal Reynolds number are described by the same solutions to the Navier–Stokes equations. We investigate resolutions ranging from 6 to 50 cells across the channel width, for two choices of the Reynolds number, Re = 30 and 3 (for $L = 25a_0$, these choices correspond to gravitational constants $g = 0.01g_0$ and $g = 0.001g_0$). As shown in the inset of figure 3, slip decreases with increasing resolution (albeit at a rate that is weakly dependent on Re), with $\mathrm{Kn} < 10^{-3}$ for the largest resolution studied at Re = 30. This confirms that spurious slip in the MPC method can also be mitigated by increasing the cell resolution, although it must be noted that this is a computationally demanding approach. Our simulation for $L/a_0 = 50$ involved 8×10^6 fluid particles.

7. Partial slip at the surface of particles in motion

7.1. Thermal behavior

We now proceed to test the mixed bounce-back conditions for partial slip at the surface of mobile colloidal particles. We consider three different approaches: (i) Method 1 (cf section 4.3) for the mixed bounce-back conditions, in combination with pseudoparticles to remove spurious slip; (ii) Method 1, without employing pseudoparticles; (iii) Method 2, again without pseudoparticles.

Since energy and momentum conservation are affected by Method 1 and also require particular attention when pseudoparticles are used (cf section 5.3), we first investigate the thermal properties of a single colloid of radius $a = 2a_0$ and mass $M_c = 125m_f$, diffusing in a cubic system of linear dimension $L = 24a_0$. The system is filled with an MPC-AT fluid with $\lambda = 0.1$ and $\gamma = 5$. We perform 10^6 MD time steps of length $0.025t_0$, for different choices of Γ. For all cases, we determine the distributions of linear and angular momentum of the colloid, and compare these to the expected Maxwell–Boltzmann distributions.

In figure 4, we show the results obtained using Method 1, with pseudoparticles placed according to the VPC. The momentum change experienced by the pseudoparticles in the collision step is transferred to the colloid, in accordance with equations (14) and (15). This leads to serious deviations in the thermal behavior, as is evident from the velocity distributions. With increasing Γ, the pseudoparticle velocities (equation (12)) become less determined by the colloid velocity and more by the velocity of the real fluid particles, leading to a larger momentum transfer to the colloid and more pronounced overheating of the colloid. The seriousness of this effect becomes particularly evident if one realizes that the fluid–colloid coupling should *decrease*, rather than increase, with increasing Γ.

Based upon these findings, we repeat the simulation utilizing Method 1 without pseudoparticles. For pure stick boundary conditions ($\Gamma = 0$) the velocity distributions (figure 5) match the theoretical predictions, and also for pure slip boundary conditions ($\Gamma = 1$) the linear velocity distribution shows excellent agreement. However, for intermediate values ($\Gamma = 0.25, 0.50, 0.75$) pronounced cooling effects are observed, as borne out by distributions that are more narrow than expected. These effects are particularly strong for the angular velocity distribution at $\Gamma = 0.75$. The origin of this discrepancy lies in the dissipative interactions at the colloidal surface, which lead to violation of energy conservation.

Lastly, to overcome the deficiencies observed in figures 4 and 5, we perform the diffusion simulation using Method 2 (probabilistic mixing of stick and slip behavior) without pseudoparticles. Since all fluid–colloid collisions now conserve energy, the distributions shown in figure 6 agree with the theoretical prediction for all choices of Γ. Although Method 2 used without pseudoparticles is still susceptible to spurious slip resulting from underfilled cells, we consider this

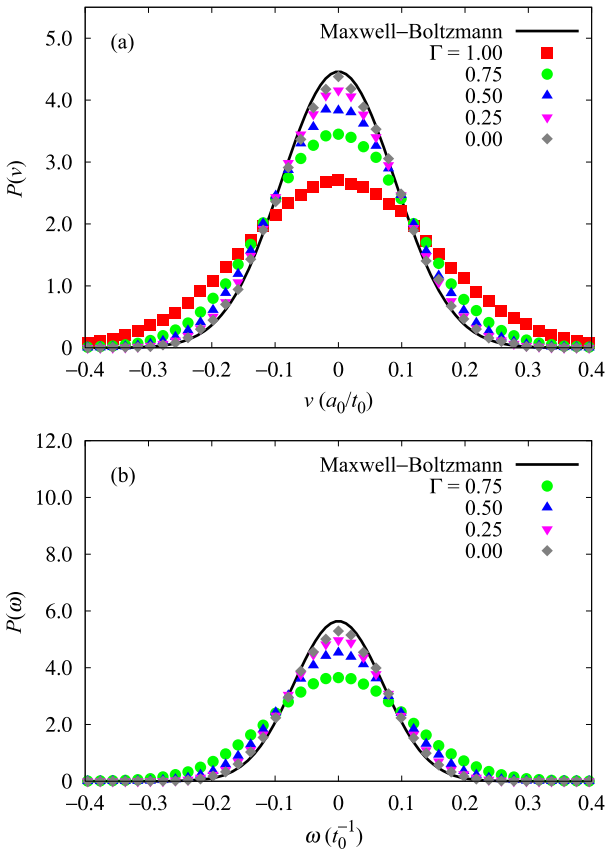

Figure 4. Distribution of (a) linear and (b) angular velocity of a colloid (radius $a = 2a_0$, mass $M_c = 125m_f$) suspended in an MPC-AT fluid, for different choices of the slip length at the colloidal surface. The system size is $L = 24a_0$ and the fluid particle density $\gamma = 5$. The simulations employ Method 1 for the mixed bounce-back conditions (section 4.3), in combination with the VPC (section 5.2) to eliminate spurious slip. For all values of the slip coefficient Γ, the simulation results deviate from the expected Maxwell–Boltzmann distribution. Note that $P(\omega)$ is omitted for $\Gamma = 1.0$, since the angular momentum of the colloid cannot be affected by the fluid in case of perfect slip.

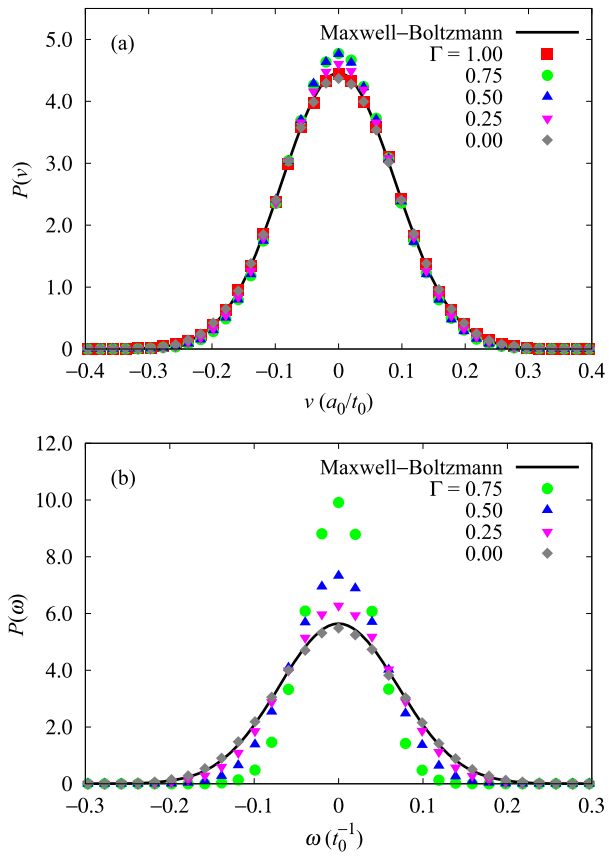

Figure 5. Distribution of (a) linear and (b) angular colloidal velocity, for the same parameters as in figure 4. The simulations employ Method 1 for the mixed bounce-back conditions, without using any pseudoparticles. For $\Gamma \notin \{0, 1\}$, the presence of dissipative interactions at the colloid surface decreases its effective temperature, reflected in velocity distributions that are too narrow compared to the Maxwell–Boltzmann distribution.

the method of choice because of its proper representation of the thermal behavior of the colloid.

7.2. Drag forces

We still have to determine how well slip can be controlled at spherical surfaces using mixed bounce-back conditions (which we now exclusively implement using Method 2), in particular because our findings in section 7.1 indicate that it is preferable to omit pseudoparticles. Here, we address this question by varying the slip coefficient Γ and determining the effect on the particle drag. In low Reynolds number flow, a spherical particle with stick boundary conditions experiences a uniform hydrodynamic drag force,

$$\mathbf{F}_{\text{drag}} = -\zeta_{\mathbf{v}}\mathbf{v}, \tag{20}$$

where $\zeta_{\mathbf{v}} = 6\pi\eta a$ [24, 43] varies linearly with both the fluid viscosity η and the colloidal radius a. For slip boundary conditions, the same equation holds, with $\zeta_{\mathbf{v}} = 4\pi\eta a$. Partial slip conditions interpolate between these two values. To measure the drag of a colloid with partial slip boundary conditions we study sedimentation of a set of eight colloids in a periodic box of dimensions $L \times L \times 3L$, where $L = 32a_0$. Both the MPC fluid and the colloids are identical to those employed in section 7.1. Colloid–colloid interactions are represented by a steep, purely repulsive potential,

$$\frac{U(r)}{k_B T} = 10\left[\left(\frac{\sigma_{cc}}{r}\right)^{48} - \left(\frac{\sigma_{cc}}{r}\right)^{24}\right] + \frac{5}{2} \quad \text{for } r < 2^{1/24}\sigma_{cc}. \tag{21}$$

The colloid–colloid diameter is set to $\sigma_{cc} = 2.15a$, i.e., slightly larger than the colloidal diameter $2a$ as seen by the fluid particles, to ensure that fluid particles do not simultaneously overlap with multiple colloids (cf section 4.1). The colloid volume fraction is small enough that mutual hydrodynamic effects are unimportant [8], so that the sedimentation velocity is inversely proportional to the single-particle drag. We choose the Péclet number $\text{Pe} = M_c g a / k_B T = 10$ to rapidly obtain a steady-state sedimentation velocity.

Figure 7 illustrates that the sedimentation velocity increases with increasing Γ, in accordance with the decreasing

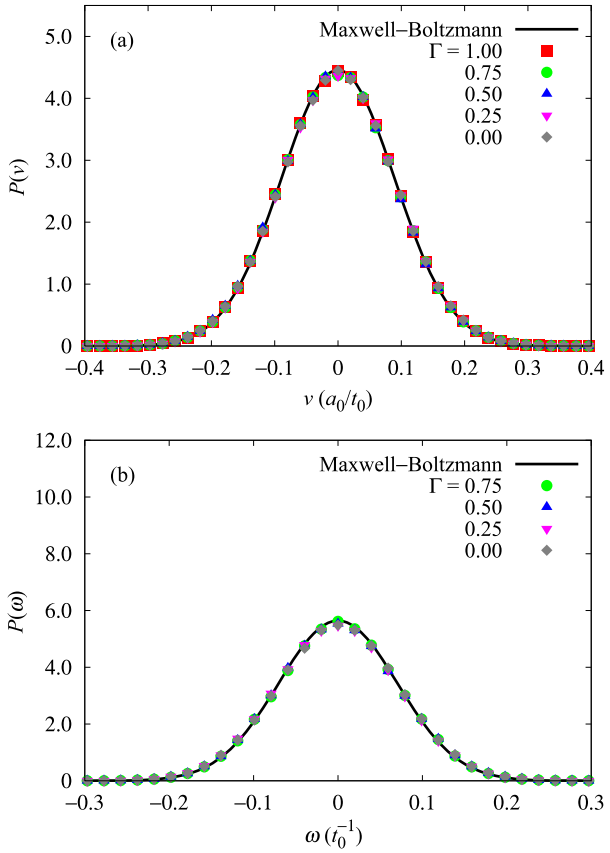

Figure 6. Distribution of (a) linear and (b) angular colloidal velocity, for the same parameters as in figure 4. The simulations disregard pseudoparticles (to avoid the deviations exhibited in figure 4) and use the energy conserving mixed bounce-back conditions according to Method 2 (to avoid the deviations found in figure 5). For all choices of the slip parameter Γ the thermal behavior of the colloid agrees with the analytical prediction.

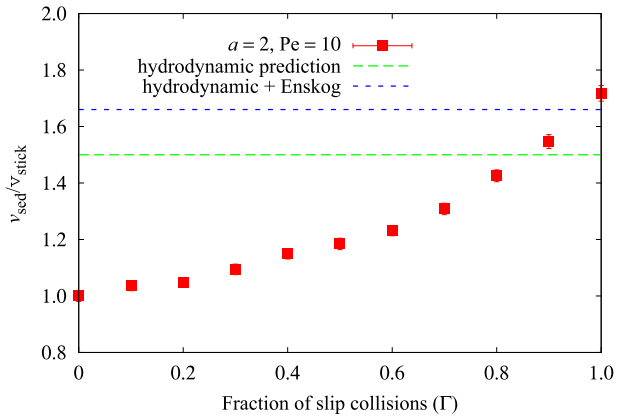

Figure 7. Sedimentation velocity of colloids of radius $a = 2a_0$, as a function of the slip coefficient Γ. The colloids settle under the influence of a gravitational force characterized by a Péclet number $\mathrm{Pe} = 10$. Sedimentation velocities are determined by block averaging, and normalized by the measured velocity at $\Gamma = 0$ (stick boundary conditions). The lines indicate the slip ratio (3/2) expected from continuum hydrodynamics and the slip ratio adjusted for Enskog effects (cf equation (22)).

drag as the degree of slip increases. Although a velocity increase by a factor 3/2 is expected from continuum hydrodynamics if Γ is varied from 0 to 1, our simulations exhibit an increase by a factor 1.7. It should be noted that in our system, due to the coarse-graining of length scales inherent in the MPC method [22], there are two appreciable sources of friction. The short-time dynamics are dominated by the ballistic collisions between the colloid and fluid particles, which can be described by Enskog dense-gas kinetic theory [22, 37, 39, 44–47]. The long-time behavior, on the other hand, is dominated by hydrodynamic effects. If one assumes that these timescales are well separated, an estimate for the total friction coefficient of fluid acting on a colloidal particle can be obtained from the Green–Kubo relation for the self-diffusion coefficient of the colloid,

$$\begin{aligned} D_{\mathrm{self}} &= \frac{k_{\mathrm{B}}T}{\zeta_{\mathbf{v}}} = \frac{1}{3}\int_0^\infty \mathrm{d}t\,\langle \mathbf{v}(t)\cdot\mathbf{v}(0)\rangle \\ &\approx \frac{1}{3}\int_0^\infty \mathrm{d}t\,(\langle \mathbf{v}(t)\cdot\mathbf{v}(0)\rangle_{\mathrm{E}} + \langle \mathbf{v}(t)\cdot\mathbf{v}(0)\rangle_{\mathrm{H}}) \\ &\approx \frac{k_{\mathrm{B}}T}{\zeta_{\mathbf{v},\mathrm{E}}} + \frac{k_{\mathrm{B}}T}{\zeta_{\mathbf{v},\mathrm{H}}}. \end{aligned} \tag{22}$$

Thus, the total friction can be estimated by summing the Enskog (subscript E) and hydrodynamic (subscript H) frictions in parallel [22, 37]. Using an explicit calculation of the Enskog contribution (see appendix B) we find that the sedimentation velocity increases by a factor 1.66 when Γ is increased from 0 to 1, in closer agreement with the results of figure 7. We expect that a more accurate accounting for the crossover between Enskog and hydrodynamic effects, and subsequent integration of the velocity autocorrelation function, would further improve the agreement.

7.3. Friction and autocorrelation functions

The crossover between Enskog and hydrodynamic behavior can be explicitly shown by examining the autocorrelation functions of velocity and angular velocity for colloids embedded in an MPC fluid [37]. Under the same assumptions as in section 7.2, equivalent forms to equations (20) and (22) are satisfied for the rotational degrees of freedom, with $\zeta_{\omega,\mathrm{H}}$ equal to $8\pi\eta a^3$ for stick conditions and equal to 0 for slip conditions.

At long times, the autocorrelation functions are described by hydrodynamic mode-coupling theory (MCT), which predicts that the autocorrelation functions for the linear and angular velocity exhibit a power-law decay [37, 48],

$$\lim_{t\to\infty}\langle v(t)v(0)\rangle = \frac{k_{\mathrm{B}}T}{12m_{\mathrm{f}}\gamma[\pi a_0^{-2}(\nu + D_{\mathrm{self}})t]^{3/2}}, \tag{23}$$

$$\lim_{t\to\infty}\langle \omega(t)\omega(0)\rangle = \frac{\pi k_{\mathrm{B}}T}{m_{\mathrm{f}}\gamma[4\pi a_0^{-2}(\nu + D_{\mathrm{self}})t]^{5/2}}, \tag{24}$$

where $\nu = \eta/\rho$ is the kinematic viscosity. Any dependence on Γ can only enter through the self-diffusion constant. However, in our systems $D_{\mathrm{self}} \ll \nu$, so that these effects are negligibly small. Consequently, the MCT result applies to both stick and partial slip boundary conditions at late times [48, 49], independent of Γ.

The short-time Enskog friction coefficients for the rotational and translational degrees of freedom of a colloidal particle in an MPC fluid are derived in appendix B. For $M_c/m_f \to \infty$ they reduce to equations (B.13) and (B.14),

$$\zeta_{v,E} = \tfrac{8}{3}\sqrt{2\pi k_B T m_f}\gamma a^2(2-\Gamma), \tag{25}$$

$$\zeta_{\omega,E} = \frac{8}{3}\sqrt{2\pi k_B T m_f}\gamma a^2 \frac{1-\Gamma}{\chi}. \tag{26}$$

In these expressions, $\chi = 2/5$ is the gyroscopic ratio for uniform spheres. This friction describes the initial exponential decay rate of the correlation function.

We examine the velocity autocorrelation functions for the same system as described in section 7.1. Slip is controlled via Method 2 without pseudoparticles, with values for $\Gamma \in [0, 1]$, spaced at intervals of 0.2. To properly resolve the long-time behavior, the runs are performed for 10^8 time steps. The results for three representative choices of Γ (0.0, 0.6, 1.0) are shown in figure 8. The short-time behavior of both the linear and the angular velocity is in excellent agreement with the Enskog behavior of equations (25) and (26), and the simulation results exhibit the predicted Γ dependence. For longer times the autocorrelation functions cross over to the power-law decay predicted by mode-coupling theory. It should be noted that the agreement between simulation data and analytical predictions is not the result of a fit; all of the variables in equations (23)–(26) are accounted for by the parameters chosen in the MPC simulation.

We note that for the rotational friction the crossover from short-time to long-time behavior increases with increasing Γ. This is due to the fact that partial slip boundary conditions interpolate between a finite rotational drag and no rotational drag. In particular, this implies that systems in which colloidal rotational effects are important require long simulation times, to ensure that these degrees of freedom are accurately explored.

Lastly, we point out that our equations (25) and (26) are of a different form than those in [37], where the Enskog result for the rough-sphere model [39, 44, 46] was applied. As noted in appendix B, this result is inapplicable to MPC dynamics, since only the colloidal species has rotational degrees of freedom. Numerically, the rough-sphere model (which represents perfect stick boundary conditions) coincides with our equations if Γ is set to 5/7; indeed, empirically we found that our simulation data match the rough-sphere model for a slip coefficient $\Gamma \in [0.6, 0.8]$. Correspondingly, the conclusion of [37] that the rough-sphere model provides a good description of colloids simulated with the stochastic boundary condition (section 4.2) in fact reconfirms that such boundary conditions produce spurious slip, consistent with our findings in section 6.1.

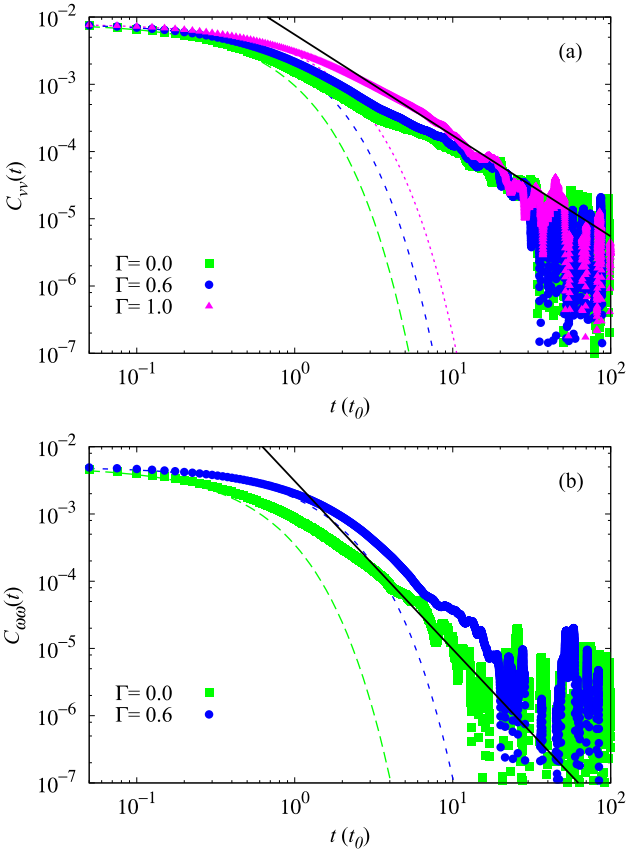

Figure 8. Autocorrelation functions $C_{xx}(t) = \langle x(t)x(0)\rangle$, for (a) the linear velocity ($x = v$) and (b) the angular velocity ($x = \omega$) of a colloid embedded in an MPC fluid. Three different boundary conditions are examined: perfect stick ($\Gamma = 0$), partial slip ($\Gamma = 0.6$), and perfect slip ($\Gamma = 1$). Parameter values are provided in the text. Dashed curves correspond to the exponential short-time decay derived from Enskog theory (appendix B) and the solid lines are the long-time power-law decay predicted by mode-coupling theory.

8. Conclusion

In conclusion, we have tested various boundary conditions for an MPC fluid interacting with solid walls or suspended solid particles. We confirmed earlier observations of apparent slip near the surface, and explicitly showed how this slip arises from a viscosity reduction resulting from the fact that boundary cells have a lower fluid particle density than bulk cells. While this can be mitigated by means of virtual particles in situations where momentum transfer at the surface does not affect the solid (e.g., massive walls), this solution leads to systematic deviations in case of thermally responsive surfaces, such as mobile colloids. Furthermore, we found that a stochastic algorithm for implementing stick boundary conditions in fact leads to significant slip in plane Poiseuille flow. These findings lead us to the conclusion that stick boundary conditions in MPC-based simulations are best represented by the bounce-back rule. When virtual particles are omitted, spurious slip can be reduced by increasing the resolution of the MPC cell grid. In addition, we have proposed an implementation of partial slip boundary conditions, in which bounce-back collisions and specular reflections are mixed on a stochastic basis. For plane Poiseuille flow we have demonstrated that this provides an accurately tunable slip length, whereas for colloids we have verified its effectiveness by means of the sedimentation velocity. Building upon earlier results, we have derived the Enskog friction describing the short-time behavior of the linear and angular velocity autocorrelation functions of a colloid embedded in an MPC fluid, and demonstrated that these results

are in good agreement with simulations employing our partial slip boundary conditions.

Acknowledgment

This material is based upon work supported by the National Science Foundation under Grant No. DMR-0346914.

Appendix A. Calculation of the collisional viscosity near a wall

Here, we calculate how the collisional viscosity (i.e., the viscosity contributed by the collision step of the MPC method) is affected by the partial filling of cells that are intersected by a solid–fluid interface. Since this is an immediate extension of the calculation presented in [29] for bulk cells, we first review the essential steps of that work, following the notation of the present paper.

Recall from equation (5) that the shear viscosity is defined by the relation

$$\sigma_{xz} = \eta \partial_z u_x, \tag{A.1}$$

so that the collisional viscosity can be computed from the stress contribution and the shear rate in the collision step.

Consider a single, cubic collision cell, with boundaries $[0, a_0]$ in all three dimensions. The cell contains n fluid particles which have a center-of-mass velocity $\mathbf{u}$, whose x-component is denoted as u_x. We define two subcells by dividing this cell with a plane at constant $z = z_0 \in [0, a_0]$. The cells $S_1 = \{z \mid 0 \leqslant z \leqslant z_0\}$ and $S_2 = \{z \mid z_0 < z \leqslant a_0\}$ have n_1 and n_2 particles, respectively, with center-of-mass velocities $u_{x,1}$ and $u_{x,2}$. Independent of z_0, the average distance between the center of mass of the two subcells is $a_0/2$, so that

$$\dot\gamma = \partial_z u_x \approx \frac{\Delta u_x}{\Delta z} = 2\frac{u_{x,2} - u_{x,1}}{a_0}. \tag{A.2}$$

Since the center-of-mass velocities in the subcells are related via $u_{x,2} = (nu_x - n_1 u_{x,1})/(n - n_1)$, the shear rate can be written as

$$\dot\gamma = \frac{2n}{a_0(n - n_1)}(u_x - u_{x,1}). \tag{A.3}$$

Next, we calculate the stress tensor from the momentum flux across the plane dividing S_1 and S_2 during the collision step,

$$\sigma_{xz} = \frac{1}{a_0^2 \Delta t_c} \sum_{i \in S_1} \Delta p_x^i, \tag{A.4}$$

where Δp_x^i is the change in x-momentum of particle i. Since the MPC operator $\mathbf{\Omega}$ affects only the particle momenta *relative* to the cell center-of-mass (cf equation (3)), we find

$$\sigma_{xz} = \frac{m_f n_1}{a_0^2 \Delta t_c}(1 - \langle \mathbf{\Omega} \rangle)(u_x - u_{x,1}), \tag{A.5}$$

where $\langle \mathbf{\Omega} \rangle$ indicates the average over all realizations of the collision operator. Substitution of equations (A.3) and (A.5) in equation (A.1) yields the viscosity due to the collision step,

$$\eta_{\mathrm{col}} = \frac{m_f n_1}{a_0^2 \Delta t_c}(1 - \langle \mathbf{\Omega} \rangle)\frac{a_0}{2}\frac{n - n_1}{n}. \tag{A.6}$$

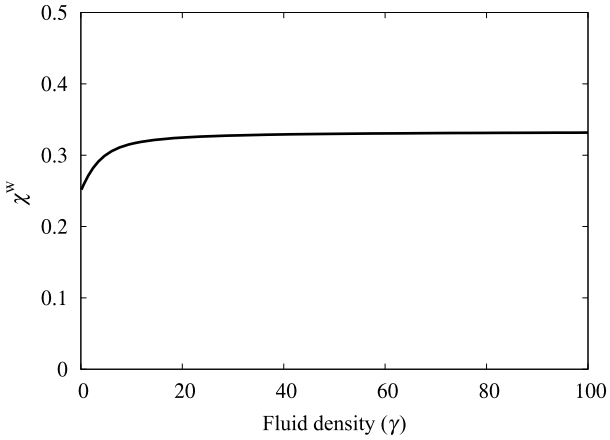

Figure A.1. Ratio χ^w of the collisional viscosity in boundary cells, η_{col}^w, to the bulk collisional viscosity, η_{col}, for MPC simulations, as a function of the average number of fluid particles per cell, γ.

Since the number of particles in the cell is typically small, we must take into account fluctuations. For a given value of n, n_1 is binomially distributed with probability $p = z_0/a_0$. Using the binomial mean $\langle n_1 \rangle = np$ and variance $\langle (n_1 - \langle n_1 \rangle)^2 \rangle = np(1 - p)$, we obtain

$$\eta_{\mathrm{col}} = \frac{m_f(n-1)}{2a_0 \Delta t_c}(1 - \langle \mathbf{\Omega} \rangle)\left(\frac{z_0}{a_0}\right)\left(1 - \frac{z_0}{a_0}\right). \tag{A.7}$$

The total number of particles in the cell fluctuates as well and, for large enough systems, will follow a Poisson distribution with mean γ. If, in addition, we average over the position z_0 of the dividing plane, we recover equation (14) of [29],

$$\eta_{\mathrm{col}} = \frac{m_f}{12a_0 \Delta t_c}(1 - \langle \mathbf{\Omega} \rangle)[\gamma - 1 + \mathrm{e}^{-\gamma}]. \tag{A.8}$$

In the presence of a wall at $z = z_w$, particles are excluded from the region $[0, z_w]$ and the location z_0 of the dividing plane between the two subcells must be chosen in the range $[z_w, a_0]$. Thus, in equation (A.3) the average center-of-mass distance $a_0/2$ between the subcells is replaced by $(a_0 - z_w)/2$. The binomial distribution of n_1 has a probability $p = (z_0 - z_w)/(a_0 - z_w)$ so that equation (A.7) is replaced by

$$\eta_{\mathrm{col}}^w = \frac{m_f(n-1)}{a_0^2 \Delta t_c}\left(\frac{a_0 - z_w}{2}\right)(1 - \langle \mathbf{\Omega} \rangle) \times \left(\frac{z_0 - z_w}{a_0}\right)\left(1 - \frac{z_0 - z_w}{a_0}\right). \tag{A.9}$$

Upon averaging over the particle number, which now has a lower mean value $\gamma' = \gamma(a_0 - z_w)/a_0$, and over z_0, we find

$$\eta_{\mathrm{col}}^w = \frac{m_f}{12a_0 \Delta t_c}\frac{(a_0 - z_w)}{a_0}(1 - \langle \mathbf{\Omega} \rangle) \times \left(\gamma \frac{a_0 - z_w}{a_0} - 1 + \mathrm{e}^{-\gamma \frac{a_0 - z_w}{a_0}}\right). \tag{A.10}$$

Finally, we integrate over all wall positions z_w to obtain the collisional viscosity in a boundary cell,

$$\eta_{\mathrm{col}}^w = \frac{m_f}{12a_0 \Delta t_c}(1 - \langle \mathbf{\Omega} \rangle)\left[\frac{\gamma}{3} - \frac{1}{2} + \frac{1 - (1+\gamma)\mathrm{e}^{-\gamma}}{\gamma^2}\right]. \tag{A.11}$$

Comparison of the factor in square brackets in equations (A.8) and (A.11) shows that, in the limit of a large number of fluid particles per MPC cell, the collisional viscosity is reduced to 1/3 of its bulk value, explaining the occurrence of spurious slip near walls. As illustrated in figure A.1, $\eta_{\mathrm{col}}^{\mathrm{w}}$ is reduced even more for values of γ that are typical in actual simulations.

Appendix B. Corrections to Enskog friction for the MPC model

The short-time ballistic behavior of colloids in an MPC solvent is well described by Enskog kinetic theory for smooth spheres when colloid–solvent interactions do not transfer angular momentum. When bounce-back conditions are used, rotational degrees of freedom must be accounted for. One might interpret bounce-back collisions as interactions between rough spheres, and use the rough-sphere result to determine the short-time behavior under stick boundary conditions, but this is conceptually incorrect. The strength of friction depends on the impulse received by a colloid during a collision with an MPC particle. Application of the rough-sphere result tacitly assumes that the MPC particle has a moment of inertia. Since MPC particles are point particles, such an assumption leads to incorrect results. Using conservation of momentum together with previous results [39, 44–47], we show here that properly accounting for the lack of rotational inertia in the MPC particle leads to a corrected equation which is mathematically similar to the rough-sphere result, but includes a multiplicative factor that is the ratio between the colloidal mass and the MPC fluid particle mass.

We start from the equations for momentum conservation. The vector $\hat{\mathbf{n}}$ is defined as the unit vector pointing from the center of the colloid to the point of contact between the colloid and the fluid particle. We denote the fluid mass by m_{f}, and the colloid mass and moment of inertia by M_{c} and I_{c}, respectively. The linear and angular velocities of the fluid particle and the colloid are distinguished by means of the subscripts f and c. The impulse $\mathbf{J}$ exerted on the colloid in a collision then satisfies

$$m_{\mathrm{f}}\mathbf{v}_{\mathrm{f}}' = m_{\mathrm{f}}\mathbf{v}_{\mathrm{f}} - \mathbf{J}, \tag{B.1}$$

$$M_{\mathrm{c}}\mathbf{v}_{\mathrm{c}}' = M_{\mathrm{c}}\mathbf{v}_{\mathrm{c}} + \mathbf{J}, \tag{B.2}$$

$$I_{\mathrm{c}}\boldsymbol{\omega}_{\mathrm{c}}' = I_{\mathrm{c}}\boldsymbol{\omega}_{\mathrm{c}} + a(\hat{\mathbf{n}} \times \mathbf{J}), \tag{B.3}$$

where the primed quantities denote velocities after the collision. Note that there is no equation for the angular momentum of the MPC point particle. The relative velocity at the point of contact between the two particles is

$$\tilde{\mathbf{v}} = \mathbf{v}_{\mathrm{f}} - \mathbf{v}_{\mathrm{c}} - \boldsymbol{\omega}_{\mathrm{c}} \times a\hat{\mathbf{n}}. \tag{B.4}$$

For the general case of mixed boundary conditions (section 4.3), the post-collision relative velocity is specified by equations (9) and (10) for Method 1. For Method 2, equation (10) must be interpreted as a time average. Combining these equations with equations (B.1)–(B.3) we can relate the normal and tangential components of $\mathbf{J}$ and $\tilde{\mathbf{v}}$,

$$\mathbf{J}_n = 2\mu\tilde{\mathbf{v}}_n, \tag{B.5}$$

$$\mathbf{J}_t = 2(1-\Gamma)\mu\frac{M_{\mathrm{c}}\chi}{\mu + M_{\mathrm{c}}\chi}\tilde{\mathbf{v}}_t, \tag{B.6}$$

with $\mu = (1/m_{\mathrm{f}} + 1/M_{\mathrm{c}})^{-1}$. The gyroscopic ratio $\chi = I_{\mathrm{c}}/(M_{\mathrm{c}}a^2)$ equals 2/5 for uniform spheres. Note that this is the analog of equation (4.2) of [46] for two partially slipping spheres where the constant κ_{12} in that equation has been replaced by

$$\kappa_{\mathrm{fc}} = \frac{M_{\mathrm{c}}\chi}{\mu + M_{\mathrm{c}}\chi} = \frac{\chi(M_{\mathrm{c}}/\mu)}{1 + \chi(M_{\mathrm{c}}/\mu)}. \tag{B.7}$$

Indeed, if the fluid particle were replaced by a sphere of uniform density, the ratio (M_{c}/μ) in equation (B.7) would reduce to μ/μ, recovering the result $\kappa_{12} = \chi/(1+\chi)$ of [46].

From this, we can apply exactly the methods of [39, 46], to obtain

$$\zeta_{\mathbf{v}} = \zeta_{\mathbf{v}}^{\mathrm{smooth}}\left[\frac{1 + (2-\Gamma)\chi M_{\mathrm{c}}/\mu}{1 + \chi M_{\mathrm{c}}/\mu}\right], \tag{B.8}$$

$$\zeta_{\boldsymbol{\omega}} = \zeta_{\mathbf{v}}^{\mathrm{smooth}}\frac{1}{\chi}\left[(1-\Gamma)\frac{\chi M_{\mathrm{c}}/\mu}{1 + \chi M_{\mathrm{c}}/\mu}\right], \tag{B.9}$$

where the smooth-sphere Enskog result is

$$\zeta_{\mathbf{v}}^{\mathrm{smooth}} = \tfrac{8}{3}\sqrt{2\pi k_{\mathrm{B}}T\mu}\gamma a^2. \tag{B.10}$$

Here we have omitted the subscript E used in section 7.2, since our only interest is in the Enskog contribution. As a consistency check, we confirm that for $M_{\mathrm{c}}/\mu \to 1$, equations (B.8) and (B.9) coincide with equations (5.3a) and (5.3b) of [46]. If, in addition, $\Gamma = 0$, they reduce to the rough-sphere results (equations (4.4) and (4.5) of [44]),

$$\zeta_{\mathbf{v}}^{\mathrm{rough}} = \zeta_{\mathbf{v}}^{\mathrm{smooth}}\frac{1+2\chi}{1+\chi}, \tag{B.11}$$

$$\zeta_{\boldsymbol{\omega}}^{\mathrm{rough}} = \zeta_{\mathbf{v}}^{\mathrm{smooth}}\frac{1}{1+\chi}. \tag{B.12}$$

However, for suspended colloids, the relevant limit is $M_{\mathrm{c}}/m_{\mathrm{f}} \to \infty$. Then, equations (B.8) and (B.9) reduce to

$$\zeta_{\mathbf{v}} = \zeta_{\mathbf{v}}^{\mathrm{smooth}}(2-\Gamma), \tag{B.13}$$

$$\zeta_{\boldsymbol{\omega}} = \zeta_{\mathbf{v}}^{\mathrm{smooth}}\frac{1}{\chi}(1-\Gamma). \tag{B.14}$$

Comparison of these equations to equations (B.11) and (B.12) shows that numerically our results match the rough-sphere results if we use the uniform-sphere value for χ and set $\Gamma = 5/7$. Thus, improper application of equations (B.11) and (B.12) to simulations of a colloid embedded in an MPC fluid will lead to spurious agreement in case of partial slip boundary conditions.

References

[1] Malevanets A and Kapral R 1999 *J. Chem. Phys.* **110** 8605
[2] Malevanets A and Kapral R 2000 *J. Chem. Phys.* **112** 7260
[3] Padding J T and Louis A A 2008 *Phys. Rev.* E **77** 011402
[4] Hecht M, Harting J, Bier M, Reinshagen J and Herrmann H J 2006 *Phys. Rev.* E **74** 021403

[5] Hecht M, Harting J, Ihle T and Herrmann H J 2005 *Phys. Rev.* E **72** 011408
[6] Ko S Y and Lee S H 2003 *Bull. Korean Chem. Soc.* **24** 771
[7] Lee S H and Kapral R 2005 *J. Chem. Phys.* **122** 214916
[8] Padding J T and Louis A A 2004 *Phys. Rev. Lett.* **93** 220601
[9] Moncho Jordá A, Louis A A and Padding J T 2009 arXiv:0906.3071
[10] Earl D J, Pooley C M, Ryder J F, Bredberg I and Yeomans J M 2007 *J. Chem. Phys.* **126** 064703
[11] Noguchi H and Gompper G 2007 *Phys. Rev. Lett.* **98** 128103
[12] Noguchi H and Gompper G 2006 *J. Chem. Phys.* **125** 164908
[13] Noguchi H and Gompper G 2005 *J. Phys.: Condens. Matter* **17** S3439
[14] Noguchi H and Gompper G 2004 *Phys. Rev. Lett.* **93** 258102
[15] Yeomans J M 2006 *Physica* A **369** 159
[16] Ali I and Yeomans J M 2005 *J. Chem. Phys.* **123** 234903
[17] Watari N, Makino M, Kikuchi N, Larson R G and Doi M 2007 *J. Chem. Phys.* **126** 094902
[18] Gompper G, Ihle T, Kroll D M and Winkler R G 2009 *Advanced Computer Simulation Approaches for Soft Matter Sciences III* (*Advances in Polymer Science* vol 221) (Berlin: Springer) pp 1–87
[19] Kapral R 2008 *Adv. Chem. Phys.* **140** 89
[20] Noguchi H and Gompper G 2008 *Phys. Rev.* E **78** 016706
[21] Ihle T and Kroll D M 2001 *Phys. Rev.* E **63** 020201(R)
[22] Padding J T and Louis A A 2006 *Phys. Rev.* E **74** 031402
[23] Noguchi H, Kikuchi N and Gompper G 2007 *Europhys. Lett.* **78** 10005
[24] Landau L D and Lifshitz E M 1987 *Fluid Mechanics* (*Course of Theoretical Physics* vol 6) 2nd edn (Amsterdam: Elsevier)
[25] Götze I O, Noguchi H and Gompper G 2007 *Phys. Rev.* E **76** 046705
[26] Lauga E, Brenner M P and Stone H A 2007 *Handbook of Experimental Fluid Dynamics* ed C Tropea, A Yarin and J F Foss (New York: Springer) chapter 19, pp 1219–40
[27] Ihle T, Tüzel E and Kroll D M 2006 *Europhys. Lett.* **73** 664
[28] Ihle T 2008 *J. Phys.: Condens. Matter* **20** 235224
[29] Kikuchi N, Pooley C M, Ryder J F and Yeomans J M 2003 *J. Chem. Phys.* **119** 6388
[30] Ihle T and Kroll D M 2003 *Phys. Rev.* E **67** 066705
[31] Ihle T and Kroll D M 2003 *Phys. Rev.* E **67** 066706
[32] Tüzel E, Strauss M, Ihle T and Kroll D M 2003 *Phys. Rev.* E **68** 036701
[33] Granick S, Zhu Y and Lee H 2003 *Nat. Mater.* **2** 221
[34] Lauga E and Cossu C 2005 *Phys. Fluids* **17** 088106
[35] Lamura A, Gompper G, Ihle T and Kroll D M 2001 *Europhys. Lett.* **56** 319
[36] Ladd A J C and Verberg R 2001 *J. Stat. Phys.* **104** 1191
[37] Padding J T, Wysocki A, Löwen H and Louis A A 2005 *J. Phys.: Condens. Matter* **17** S3393
[38] Inoue Y, Chen Y and Ohashi H 2002 *J. Stat. Phys.* **107** 85
[39] Berne B J and Montgomery J A 1976 *Mol. Phys.* **32** 363
[40] Ahmed N K and Hecht M 2009 arXiv:0907.2877
[41] Lamura A and Gompper G 2002 *Eur. Phys. J.* E **9** 477
[42] Allahyarov E and Gompper G 2002 *Phys. Rev.* E **66** 036702
[43] Batchelor G K 1967 *An Introduction to Fluid Dynamics* (Cambridge: Cambridge University Press)
[44] Subramanian G and Davis H T 1975 *Phys. Rev.* A **11** 1430
[45] O'Dell J and Berne B J 1975 *J. Chem. Phys.* **63** 2376
[46] Berne B J 1977 *J. Chem. Phys.* **66** 2821
[47] Pangali C S and Berne B J 1977 *J. Chem. Phys.* **67** 4571
[48] Montgomery J A Jr and Berne B J 1977 *J. Chem. Phys.* **67** 4580
[49] Montgomery J A Jr and Berne B J 1977 *J. Chem. Phys.* **66** 2770